



Multiscale investigations of europium(III) complexation with tetra-*n*-octyl diglycolamide confined in porous solid supports

Journal:	<i>CrystEngComm</i>
Manuscript ID	CE-ART-07-2020-000956.R1
Article Type:	Paper
Date Submitted by the Author:	10-Sep-2020
Complete List of Authors:	Bertelsen, Erin; Colorado School of Mines, Chemistry Kovach, Nolan; Colorado School of Mines, Chemistry Reinhart, Benjamin; Argonne National Laboratory Trewyn, Brian; Colorado School of Mines, Chemistry Antonio, Mark; Argonne National Laboratory, Chemical Sciences & Engineering Division Shafer, Jenifer ; Colorado School of Mines, Department of Chemistry and Geochemistry

ARTICLE

Multiscale investigations of europium(III) complexation with tetra-*n*-octyl diglycolamide confined in porous solid supports

Received 00th January 20xx,
Accepted 00th January 20xx

Erin R. Bertelsen,^a Nolan C. Kovach,^a Benjamin J. Reinhart,^b Brian G. Trewyn,^{a,c} Mark R. Antonio^d and Jenifer C. Shafer^{a,e*}

DOI: 10.1039/x0xx00000x

The microscopic, short-range coordination environments and mesoscopic, long-range structures of Eu³⁺ contacted with tetra-*n*-octyl diglycolamide (TODGA) confined on ordered mesoporous carbon (OMC) nanoparticles and Amberchrom CG-71 resin were probed using Eu L₃-edge extended X-ray absorption fine structure (EXAFS) as well as small-angle and wide-angle X-ray scattering, SAXS and WAXS, respectively. A homoleptic Eu(TODGA)₃³⁺ coordination complex typical of liquid-liquid extraction (LLE) chemistry is present under low Eu³⁺ loading conditions on both solid supports. Deviations from this traditional structure motif appear at hyperstoichiometric Eu³⁺ loadings, above the 1:3 Eu³⁺ to TODGA mole ratio. Microcrystalline-like domains with multinuclear Eu speciation are templated by use of these high Eu³⁺ loading conditions with the functionalized OMC materials, highlighting a major departure of liquid-solid extraction chromatography (EXC) from the coordination chemistry of LLE. No such long-range spatial coherence was observed for analogous polyacrylic resin materials. These results demonstrate both the similarities and differences between multiscale structures in LLE and EXC, underscoring the opportunities for improved separation techniques based on solid supports with long-range spatial coherence (e.g., OMC systems) and without it (e.g., resin materials). Since crystallization was the first approach to adjacent lanthanide separations, the prospect of templating microcrystalline TODGA-lanthanide complexes that are otherwise not prone to crystallization by use of OMC nanoparticles represents a new entry to addressing long-standing issues in purification by liquid-solid phase separation.

Introduction

The earliest lanthanide separations were completed using fractional crystallization.^{1, 2} Crystallization in lanthanide separations works because the crystalline framework imparts significant rigidity and therefore high specificity for a given lanthanide in the crystalline matrix. Crystallization is inherently limited as a separations approach because of the inability to run this process fluidly in multiple separation stages, such as liquid-liquid extraction (LLE) or extraction chromatography (EXC). The ability to complete *in situ* crystallization coupled to a separations approach that allows for multiple separations stages would be a fundamentally different, and potentially improved, approach to lanthanide separations. The challenge is the long alkyl-chained extractants useful for industrial *f*-element solvent extraction are inherently resistant to crystallization, as precipitation in a solvent extraction process is undesirable.

In LLE and EXC chemical separation systems, tetra-*n*-octyl diglycolamide (TODGA, Figure 1) shows an unusually high efficiency and selectivity for the intra-lanthanide and trivalent actinide separations.³⁻⁶ Consequently, this extractant is extensively studied for nuclear fuel reprocessing in ALSEP (Actinide Lanthanide SEparation),⁷⁻¹⁰ EURO-GANEX,¹⁰⁻¹³ and innovative-SANEX^{10, 14-16} processes. Recent studies have shown that TODGA forms trefoil-like complexes with trivalent lanthanides and plutonium(IV) in aliphatic diluents with water and counter anions occupying the outer coordination sphere.¹⁷⁻²¹ The common structural motif is composed of three neutral TODGA molecules coordinated in a homoleptic, tridentate manner to trivalent and tetravalent cations, M(TODGA)₃³⁺ and M(TODGA)₃⁴⁺, respectively (where M = Ln³⁺, An³⁺ and An⁴⁺).^{17, 19, 20, 22-24} The coordination properties of LLE systems—such as the homoleptic metal cation TODGA structural motif—are often extended to EXC systems by presumption.

In aliphatic solvents, TODGA is prone to organization into small aggregates of the reverse micellar type upon contact with an aqueous phase.²⁵⁻²⁸ The intermolecular forces required to form TODGA aggregates larger than dimers are negligible in dry aliphatic media alone. In the absence of a diluent—along with the additional confinement within a porous material—the preorganization of TODGA may be promoted, or limited, before aqueous contact. By confining TODGA in porous solid materials designed for EXC, the extraction environment can be controlled. Accordingly, TODGA was confined on solid supports, including

^a Department of Chemistry, Colorado School of Mines, Golden, CO 80401, USA

^b Advanced Photon Source, Argonne National Laboratory, Argonne, IL 60439, USA

^c Material Science Program, Colorado School of Mines, Golden, CO 80401, USA

^d Chemical Sciences & Engineering Division, Argonne National Laboratory, Argonne, IL 60439, USA

^e Nuclear Science and Engineering Program, Colorado School of Mines, Golden, CO 80401, USA

*Corresponding author email: jshafer@mines.edu

Electronic Supplementary Information (ESI) available: [details of any supplementary information available should be included here]. See DOI: 10.1039/x0xx00000x

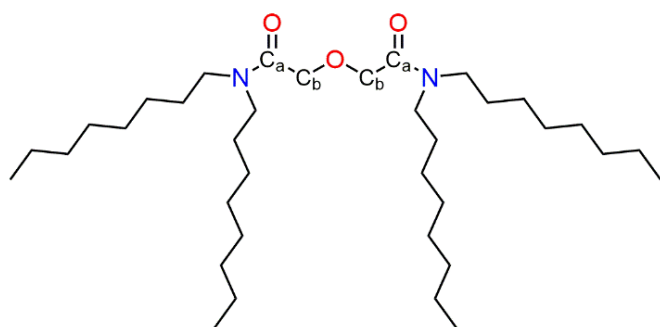


Figure 1. Structure for tetra-*n*-octyl diglycolamide (TODGA) showing the four oleophilic octyl tail groups and the hydrophilic head group consisting of nitrogen and oxygen atoms of the amide functionalities bridged by the ether O linkage. The carbonyl sp^2 -hybridized carbons and ether sp^3 -hybridized carbons are labeled C_a and C_b , respectively. Hydrogen atoms are omitted for clarity.

ordered mesoporous carbon (OMC) nanoparticles and Amberchrom CG-71 resin, with and without a phase modifier, 2-octanol. The addition of 2-octanol to TODGA increases the wettability of the oleophilic octyl tail groups of the extractant, acting as a dispersant. The modifier also mimics the solvent modification in LLE systems for third-phase prevention.²⁹ It has been suggested that an alcoholic diluent increases the dielectric constant, limiting the aggregation of TODGA thus preventing undesirable bulk phase behaviors.^{10, 30-32}

Although several similarities to LLE systems exist, there are distinct overarching deviations from the analogous EXC systems. Two characteristics are of note: First, the EXC systems do not contain an aliphatic organic diluent. The carbon-based solid support materials, however, may behave as a bulk diluent, with OMC primarily composed of sp^2 -hybridized, graphitic carbon and Amberchrom CG-71 a polymeric ester-based resin composed of sp^2 - and sp^3 -hybridized carbon.^{33, 34} Second, the TODGA extractant in the EXC systems is confined within solid, porous media as opposed to free dispersion in bulk fluid media. Given the amphiphilic nature of TODGA (Figure 1), the nonpolar oleophilic octyl chains likely orient towards the oleophilic support material and the polar hydrophilic head group faces away from the solid surface creating a hydrophilic region—without aggregation. The details of this scenario, of course, are dependent upon particle surface area, pore diameter and volume, and extractant surface coverage.

After contacting the OMC nanoparticles and resin materials with Eu^{3+} , the structures of the TODGA-confined support materials were probed by use of synchrotron radiation methods. These include extended X-ray absorption fine structure (EXAFS) spectroscopy to reveal the short-range (microscopic) coordination environments of Eu. In addition, small-angle X-ray scattering (SAXS) and wide-angle X-ray scattering (WAXS) were used to probe the long-range (mesoscopic) structures. This multiscale approach improves our understanding of the system structures. Comparison of the results with unconfined Eu in bulk solution phases from LLE, and between the two different EXC materials, provides a systematic understanding of the effects of confinement on Eu coordination chemistry.

Experimental

Materials

Europium nitrate pentahydrate, 2-octanol, and sucrose were obtained from Sigma-Aldrich. Sulfuric acid (98%) and optima grade nitric acid were purchased from Fisher Scientific. Tetra-*n*-octyl diglycolamide (TODGA, Figure 1) was ordered from Marshallton Research Laboratories Incorporated. All chemicals were used as received. Ultrapure (> 18.2 M Ω cm) deionized water was used for all aqueous solutions and synthesis steps. All resin materials, unfunctionalized and functionalized with TODGA and TODGA/2-octanol, were kindly provided by Eichrom Technologies, LLC.

Synthesis, functionalization, and characterization of OMC

Large-pore mesoporous silica nanoparticles were prepared as a sacrificial template³⁵ for the synthesis of large-pore OMC nanoparticles³⁶ using a hard-templating method. The OMC was functionalized using a general physisorption procedure.³⁷ Here, a known amount of TODGA (or TODGA and 2-octanol) was dissolved in methanol and added to a suspension of OMC in methanol. The methanol was then removed by evaporation, leaving the extractant on the OMC. The OMC was characterized before and after functionalization using nitrogen sorption analysis and thermogravimetric analysis. Three functionalized OMC materials were synthesized: 34 wt% TODGA OMC, 22 wt% TODGA/4 wt% 2-octanol OMC, and 16 wt% TODGA/8 wt% 2-octanol OMC. A full account of the synthesis, functionalization, and characterization has been previously reported by Bertelsen et al.³⁶

Europium extraction by functionalized OMC and resin

Batch extraction of Eu^{3+} was accomplished for the three functionalized OMC materials as well as two Amberchrom GC-71 functionalized resin materials provided by Eichrom Technologies, LLC. (40 wt% TODGA resin and 24 wt% TODGA/16 wt% 2-octanol resin). Aqueous solutions were prepared from $Eu(NO_3)_3 \cdot 5H_2O$ in 1 M HNO_3 to obtain Eu^{3+} concentrations of 7×10^{-5} , 0.002, 0.005, 0.01, 0.05, 0.1, and 0.425 M. Aliquots of 9 mL were contacted with 90 mg of functionalized material in a 15 mL centrifuge tube. The samples were contacted for 60 min at ambient temperature (23 °C) followed by centrifugation at 3000 $\times g$. A fine tip transfer pipette was used to remove the supernatant aqueous phase. The Eu^{3+} -loaded material was transferred to folded weigh paper and pressed to remove excess aqueous phase. The materials were left to air dry before storing in a microcentrifuge tube for analyses.

Similar extraction studies using $^{152/154}Eu^{3+}$ were done for the functionalized materials on a smaller scale to determine the Eu^{3+} loading capacity. The uptake of $^{152/154}Eu^{3+}$ was measured by contacting 5 mg of the functionalized material with 0.495 mL of the $Eu(NO_3)_3/1$ M HNO_3 aqueous solution in addition to 5 μ L of a $^{152/154}Eu^{3+}$ (~ 3.5 mM in 0.001 M HNO_3) radiotracer.³⁸ After contacting and centrifugation, 350 μ L of the aqueous phase was taken for gross gamma counting. The Eu^{3+} radioactivity contained in the functionalized materials was determined

through delta calculation. Radiotracer contacts were only done once. The quantities found were used as benchmarks to approximate the Eu^{3+} loaded on the functionalized materials used for the small-angle and wide-angle X-ray scattering (SAXS and WAXS) and EXAFS studies.

Small-angle and wide-angle X-ray scattering

SAXS and WAXS data were collected at beamline 12-ID-B of the Advanced Photon Source at Argonne National Laboratory with an incident photon energy of 13.3 keV ($\lambda = 0.9322 \text{ \AA}$). The powder samples were contained in 1 mm diameter quartz capillary tubes. Five 1 s exposures were captured with a Perkin 3M (SAXS) and Perkin 300K (WAXS) from $0.003 \text{ \AA}^{-1} \leq q \leq 2.5 \text{ \AA}^{-1}$. The frame-to-frame intensity variations (approx. 1%) were random, indicating that the OMC and resin materials are stable and the mesostructures are not perturbed/damaged during data acquisition. The five frames were averaged and the parasitic background scattering from the capillary tube subtracted. Using NCI (National Cancer Institute) SAXS macros developed for Igor Pro (WaveMetrics), the SAXS and WAXS data were merged at a singular common scattering vector to create a combined profile. The WAXS intensity was modulated, if necessary, to meet the high q region of the SAXS data.

X-ray absorption spectroscopy

Europium L_3 -edge X-ray absorption spectra were collected at beamline 12-BM-B of the Advanced Photon Source at Argonne National Laboratory for the powders as pressed pellets or packed into 1 mm quartz capillary tubes. The incident X-ray energy (I_0) was calibrated with an Fe foil. Fluorescence data (I_f/I_0) were used when transmittance data ($\ln(I_0/I_t)$) did not produce an acceptable signal, particularly for the solids with low Eu^{3+} concentrations. Three to seven scans were recorded and averaged for each sample. The normalized X-ray absorption plots are shown in Figure S1 in the Supporting Information. All analyses were performed with EXAFSPAK as described elsewhere.¹⁹ Curve fitting for the $k^3\chi(k)$ EXAFS was done ($2.02 \leq k \leq 12.58 \text{ \AA}^{-1}$) with the phase and amplitude functions from FEFF8.0.³⁹ Scale factors were fixed at 1.0 for transmittance or 0.9 for fluorescence data. The expected resolution is 0.149 \AA and the number of independent data points is 20 ($\Delta R = 3 \text{ \AA}$).

Results and discussion

Europium extraction by TODGA functionalized OMC and resin

The initial aqueous Eu^{3+} contact concentrations ranged from tracer- (approx. 0.07 mM) to macro-quantities. The TODGA functionalized OMC and resin, with and without modification by 2-octanol, were capable of sorbing hyperstoichiometric quantities of Eu^{3+} in relation to the amount of physisorbed TODGA (see Table 1) and did not reach a maximum Eu^{3+} adsorption capacity. Recent voltammetric studies using the TODGA-functionalized OMC materials in cavity microelectrodes after contact with Eu^{3+} solutions revealed an electrode potential of $-0.79 \text{ V vs. Ag/AgCl}$ for the reduction of Eu^{3+} to Eu^{2+} .³⁶ This potential is typical of the homoleptic $\text{Eu}(\text{TODGA})_3^{3+}$ complex

as demonstrated for the $\text{Eu}(\text{TODGA})_3(\text{BiCl}_4)_3$ solid salt¹⁹ in a bulk carbon paste electrode (see Supporting Information, Figure S2). When the electrode was prepared with the functionalized OMC material loaded with Eu^{3+} (i.e., 22 wt% TODGA/4 wt% 2-octanol OMC with $670 \text{ mg Eu}^{3+} \text{ g}^{-1}$), the initial electrode potential ($-0.61 \text{ V vs. Ag/AgCl}$) was consistent with that for the reduction of the aquated $\text{Eu}(\text{III})$ cation. However, after continued use the electrode potential shifted to -0.79 V reflecting the Eu –TODGA complex. The negative potential shift as a result of Eu^{3+} complexation and stabilization⁴⁰ by TODGA indicates that the initial coordination environment under high Eu^{3+} loading conditions is unique and that the speciation is something other than the homoleptic TODGA complex. The X-ray experiments (see below) provide insights into the structure variations that result as a function of Eu -loadings on the OMC nanoparticles and resin materials.

X-ray Scattering

Functionalized OMC and resin. Prior to functionalization, the SAXS profile for OMC (see Figure 2 and Figure S3 in the supporting information) exhibits a narrow peak at 0.0756 \AA^{-1} (riding on a broad, unresolved shoulder) followed by two weakly-resolved features at 0.130 and 0.150 \AA^{-1} which suggests a 2D hexagonal pore structure with d -spacing of 83.1 \AA .⁴¹ There is no such evidence for any spatial coherence in the unfunctionalized resin material, see Figure 2. The presence of extractant (34–40 wt% TODGA and 16–24 wt% TODGA/4–16 wt% 2-octanol) changes the scattering features for both the OMC and the resin supports (Figure 2). After functionalization, the OMC pore spacing slightly increases to about 84.4 \AA ($q = 0.0744 \text{ \AA}^{-1}$) and broad scattering peaks are observed for both the OMC and the resin. The features are centered around 0.367 and 1.50 \AA^{-1} ($d = 17.1, 4.19 \text{ \AA}$ and $\text{FWHM} \approx 0.11, 0.48 \text{ \AA}^{-1}$) for the OMC and $0.0797, 0.164$ and 1.30 \AA^{-1} ($d = 78.8, 38.3, 4.83 \text{ \AA}$ and $\text{FWHM} \approx 0.0027, 0.043, 0.43 \text{ \AA}^{-1}$) for the resin. The different features present from the addition TODGA or TODGA/2-octanol are indicative of new architectures templated by the support materials.

The different support properties of the Amberchrom CG-71 and OMC materials lead to different TODGA formations and domain structures within the pores and on the surface. The OMC support has an average pore size of 5.0 nm and a surface area over $1200 \text{ m}^2 \text{ g}^{-1}$;³⁶ Amberchrom CG-71 has an average pore size of 25.0 nm and an average surface area of $500 \text{ m}^2 \text{ g}^{-1}$.⁴² The narrower pores and high surface area of the OMC may limit the TODGA to a mono- or bilayer formation and/or coverage, whereas the resin could support a more substantial liquid-like coating. The resin's capability to support a bulkier liquid phase rationalizes the features present at lower q that are absent on OMC. Modifying TODGA with 2-octanol does not affect these features, indicating that the surface coverage, preorganization, and the morphology that TODGA takes on both solid supports prior to contact with an aqueous solution or metal extraction is not significantly influenced by the modifier (cf. green, blue and pink curves in Figure 2a and green and pink curves in Figure 2b).

Table 1. Sorbed Eu^{3+} on TODGA and TODGA/2-octanol functionalized OMC and resin materials at equilibrium. Errors given are $\pm 1\sigma$ determined from the propagated error in the counting statistics. The mole ratios are best whole number approximations from the wt% TODGA and sorbed Eu^{3+} calculations.

	Initial [Eu^{3+}] (M)	Sorbed Eu^{3+} (mg g^{-1})	Eu^{3+} to TODGA mole ratio
34 wt% TODGA OMC	7×10^{-5}	1.1(8)	1:81
	0.002	12.2(3)	1:7
	0.005	15.0(4)	1:6
	0.010	10.0(3)	1:9
	0.050	28.6(7)	1:3
	0.100	73(2)	1:1
	0.425	460(10)	5:1
22 wt% TODGA/4 wt% 2-octanol OMC	7×10^{-5}	1.1(2)	1:53
	0.002	7.3(2)	1:8
	0.005	9.0(2)	1:6
	0.010	14.5(4)	1:4
	0.050	16.6(4)	1:3
	0.100	80(2)	1:1
	0.425	670(20)	12:1
16 wt% TODGA/8 wt% 2-octanol OMC	7×10^{-5}	1.0(5)	1:43
	0.002	7.0(2)	1:6
	0.005	11.1(3)	1:4
	0.010	13.2(3)	1:3
	0.050	37.1(9)	1:1
	0.100	147(4)	4:1
	0.425	530(10)	13:1
40 wt% TODGA resin	7×10^{-5}	1.0(7)	1:105
	0.002	20.3(5)	1:5
	0.005	22.5(6)	1:5
	0.010	22.3(6)	1:5
	0.050	52(1)	1:2
	0.100	89(2)	1:1
	0.425	480(10)	5:1
24 wt% TODGA/16 wt% 2-octanol resin	7×10^{-5}	1.0(4)	1:62
	0.002	17.5(4)	1:4
	0.005	20.5(5)	1:3
	0.010	25.7(6)	1:2
	0.050	43(1)	2:3
	0.100	52(1)	1:1
	0.425	580(20)	9:1

Eu³⁺ loaded functionalized OMC and resin. The SAXS data for each of the functionalized materials loaded with 1.0 or 1.1 mg $\text{Eu}^{3+} \text{g}^{-1}$ are shown in Figure 3. Several differences are apparent before and after Eu^{3+} loading. The wide-angle scattering features generally shift to slightly higher q (see SI for position details); however, a fairly significant shift to 1.34 \AA^{-1} ($d = 4.69 \text{ \AA}$) is observed for the 40 wt% TODGA resin with the addition of Eu^{3+} (Figure 3d). For the OMC material

functionalized with 34 wt% TODGA and 22 wt% TODGA/4 wt% 2-octanol (Figure 3a and b), there is a decrease in the scattering intensity with the adsorption of Eu^{3+} . The depression in scattering intensity, $I(q)$, is noted from about $0.006\text{--}0.28 \text{ \AA}^{-1}$ for 34 wt% TODGA OMC (Figure 3a) and across the entire q -range for 22 wt% TODGA/4 wt% 2-octanol OMC (Figure 3b). Conversely, the 16 wt% TODGA/8 wt% 2-octanol OMC has a generally higher scattering intensity after Eu^{3+} adsorption

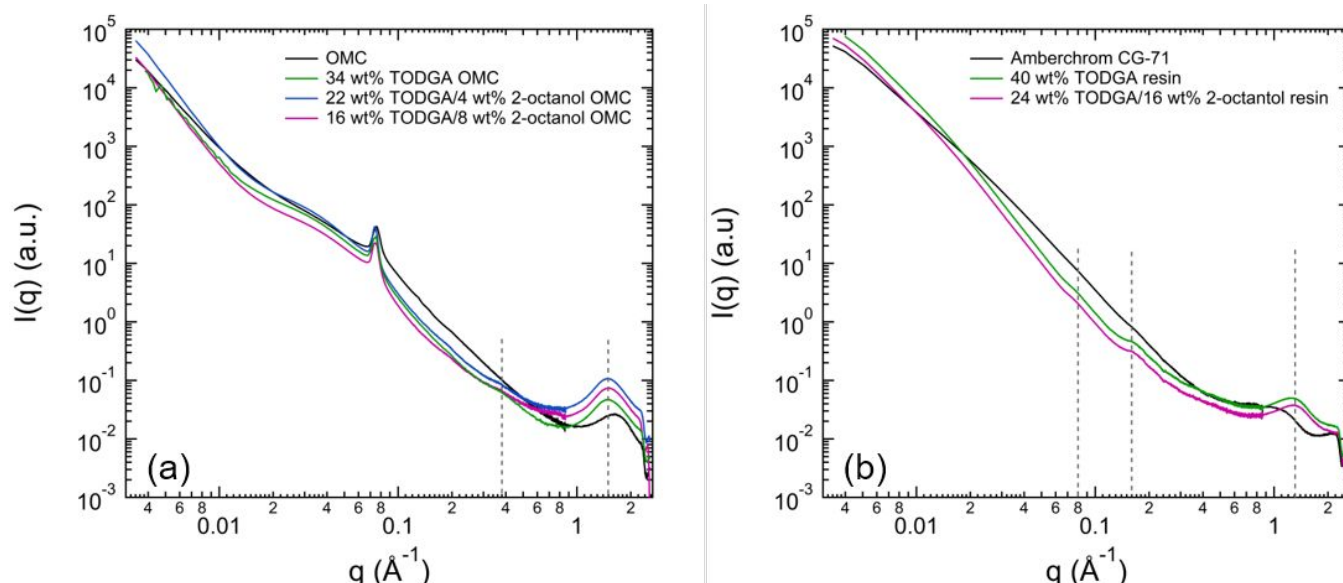


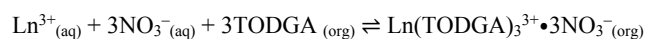
Figure 2. SAXS profiles for (a) unfunctionalized OMC (black), 34 wt% TODGA OMC (green), 22 wt% TODGA/4 wt% 2-octanol OMC (blue), and 16 wt% TODGA/8 wt% 2-octanol OMC (pink) and (b) unfunctionalized Amberchrom CG-71 (black), 40 wt% TODGA resin (green), and 24 wt% TODGA/16 wt% 2-octanol resin (pink). Peaks present after functionalization are indicated by dashed lines.

(Figure 3c). The peak present at 0.367 \AA^{-1} for all the functionalized OMC materials shifts to 0.353 \AA^{-1} ($d = 17.8 \text{ \AA}$) after initial Eu^{3+} adsorption. Both functionalized resin materials show a decrease in scattering intensity after Eu^{3+} adsorption across the SAXS region. After initial Eu^{3+} adsorption, a peak centered around 0.360 \AA^{-1} ($d = 17.5 \text{ \AA}$) emerges for both functionalized resins while the peaks at 0.0797 and 0.164 \AA^{-1} are not as predominant in the Eu^{3+} loaded 24 wt% TODGA/16 wt% 2-octanol resin (see Figure 3e). The diminution of peak intensities upon modification by 2-octanol for the resin material suggests that the presence of multilayer or microdomains of liquid-like TODGA is inhibited by the presence of Eu^{3+} in the system.

As the Eu^{3+} concentration in the materials is increased up to the stoichiometric limit of their respective TODGA concentrations, the peaks at 0.353 and 0.360 \AA^{-1} for the functionalized OMC and resin, respectively, shift to slightly lower q and become more prominent (see Figure 4). The 34 wt% TODGA OMC peak shifts to about 0.339 \AA^{-1} and the 40 wt% TODGA resin peak shifts to about 0.347 \AA^{-1} (Figure 4a and d, respectively). The shift in q (indicating increasing particle dimensions) is slightly greater with 2-octanol modification. For 22 wt% TODGA/4 wt% 2-octanol OMC (Figure 4b) and 16 wt% TODGA/8 wt% 2-octanol OMC (Figure 4c) the peak is observed at 0.336 and 0.335 \AA^{-1} , respectively. The peak for the 2-octanol modified TODGA resin is shifted to 0.342 \AA^{-1} . The 34% TODGA OMC (Figure 4a) begins to exhibit diffraction peaks. A prominent diffraction signature emerges at 0.314 \AA^{-1} (20.0 \AA) along with smaller second order peak at 0.628 \AA^{-1} (10.0 \AA) for $15.0 \text{ mg Eu}^{3+} \text{ g}^{-1}$ loading. A diffraction peak (0.310 \AA^{-1} , 20.3 \AA) with a much smaller intensity also appears in the $28.6 \text{ mg Eu}^{3+} \text{ g}^{-1}$ loaded sample. This signature diffraction peak emerges at 0.317 \AA^{-1} (19.8 \AA) in the 22 wt% TODGA/4 wt% 2-octanol OMC material (Figure 4b).

Hyperstoichiometric Eu^{3+} loaded functionalized OMC and resin. Both the functionalized OMC and resin materials were

capable of loading Eu^{3+} beyond the 1:3 Eu^{3+} to TODGA stoichiometric capacity proposed by the equilibrium equation:



This EXC overloading is remarkable by standards of LLE, wherein the organic phase saturates at the 1 Eu :3 TODGA stoichiometric limit. One way to exceed this limiting stoichiometry in LLE would be through the formation of polynuclear complexes, for which no evidence is heretofore available. The functionalized OMC materials display diffraction peaks forming past the stoichiometric loading capacity. At the highest Eu^{3+} loadings, the broad peaks centered around 0.339 , 0.336 , and 0.335 \AA^{-1} for each of the functionalized OMC materials has given way to numerous diffraction peaks throughout the high q SAXS region, extending into the WAXS region (Figure 5). All peak positions as well as slope analyses for the SAXS data are provided in Tables S1–7 in the Supporting Information.

The scattering features for the functionalized resins with the highest Eu^{3+} loadings, by contrast with the OMC systems, remain essentially consistent with those at lower Eu^{3+} loadings (Figure 5). The 40 wt% TODGA resin does have one correlation peak (0.293 \AA^{-1} , 21.4 \AA) that forms off the broad main peak (0.329 \AA^{-1} , see Figure 5d). The narrow diffraction peaks in the functionalized OMC materials' SAXS profiles indicate the presence of long-range ordering, such as resulting from the formation of a structured mesophase to microcrystalline-like domain structures. The absence of diffraction peaks for the resin materials suggest that the ordered mesopores of the OMC may be acting as a templating surface or crystal nucleation sites for the mesophase to microcrystalline-like domains—exhibiting diffraction peaks.

The characteristic diffraction peak around 0.31 \AA^{-1} (20 \AA) present for the functionalized OMC materials—signaling the transition to or the presence of a mesophase—is preceded by a prominent diffraction peak at 0.289 \AA^{-1} (21.7 \AA) at the highest

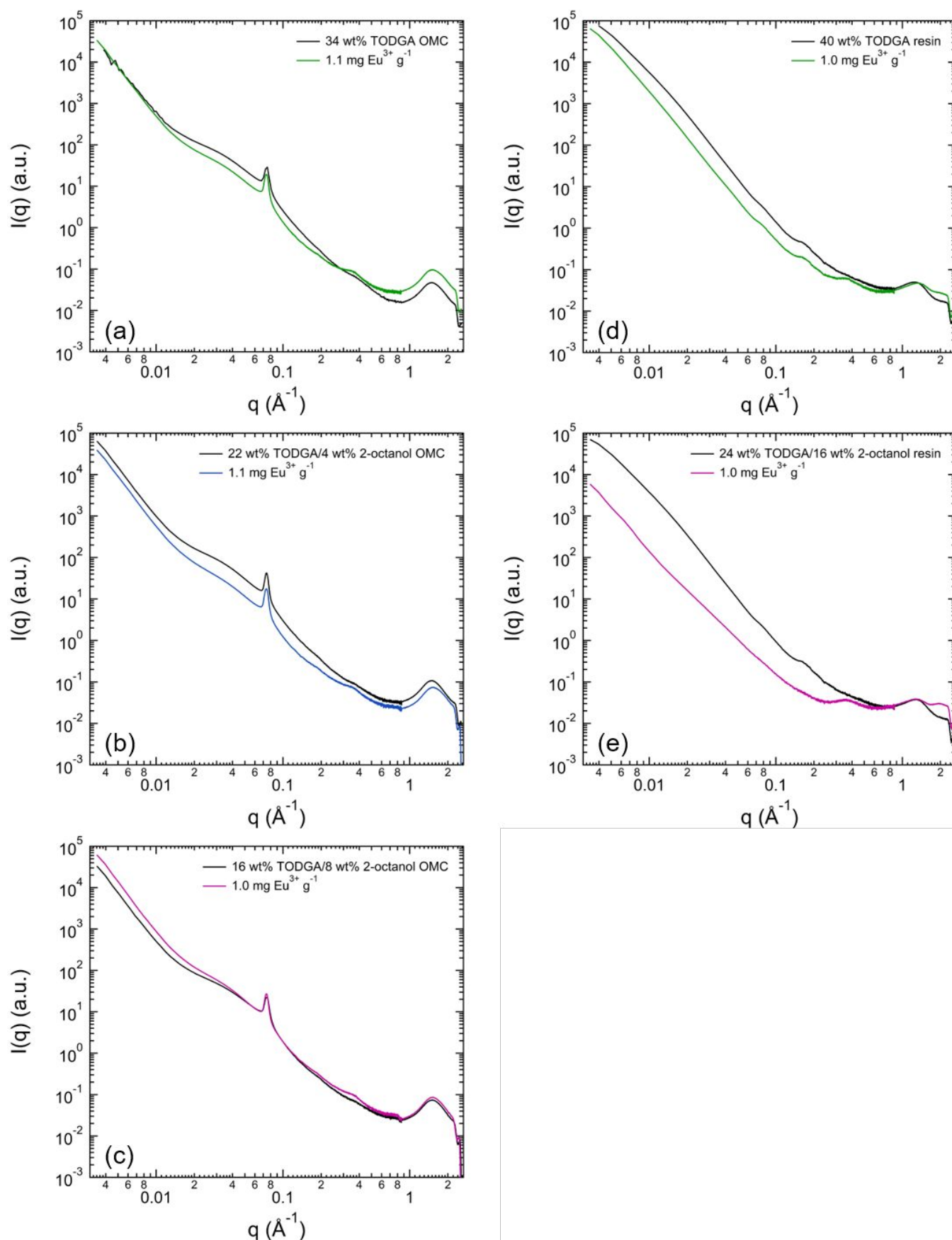


Figure 3. SAXS profiles for (a) 34 wt% TODGA OMC, (b) 22 wt% TODGA/4 wt% 2-octanol OMC, (c) 16 wt% TODGA/8 wt% 2-octanol OMC, (d) 40 wt% TODGA resin, and (e) 24 wt% TODGA/16 wt% 2-octanol resin before and after initial Eu^{3+} loading.

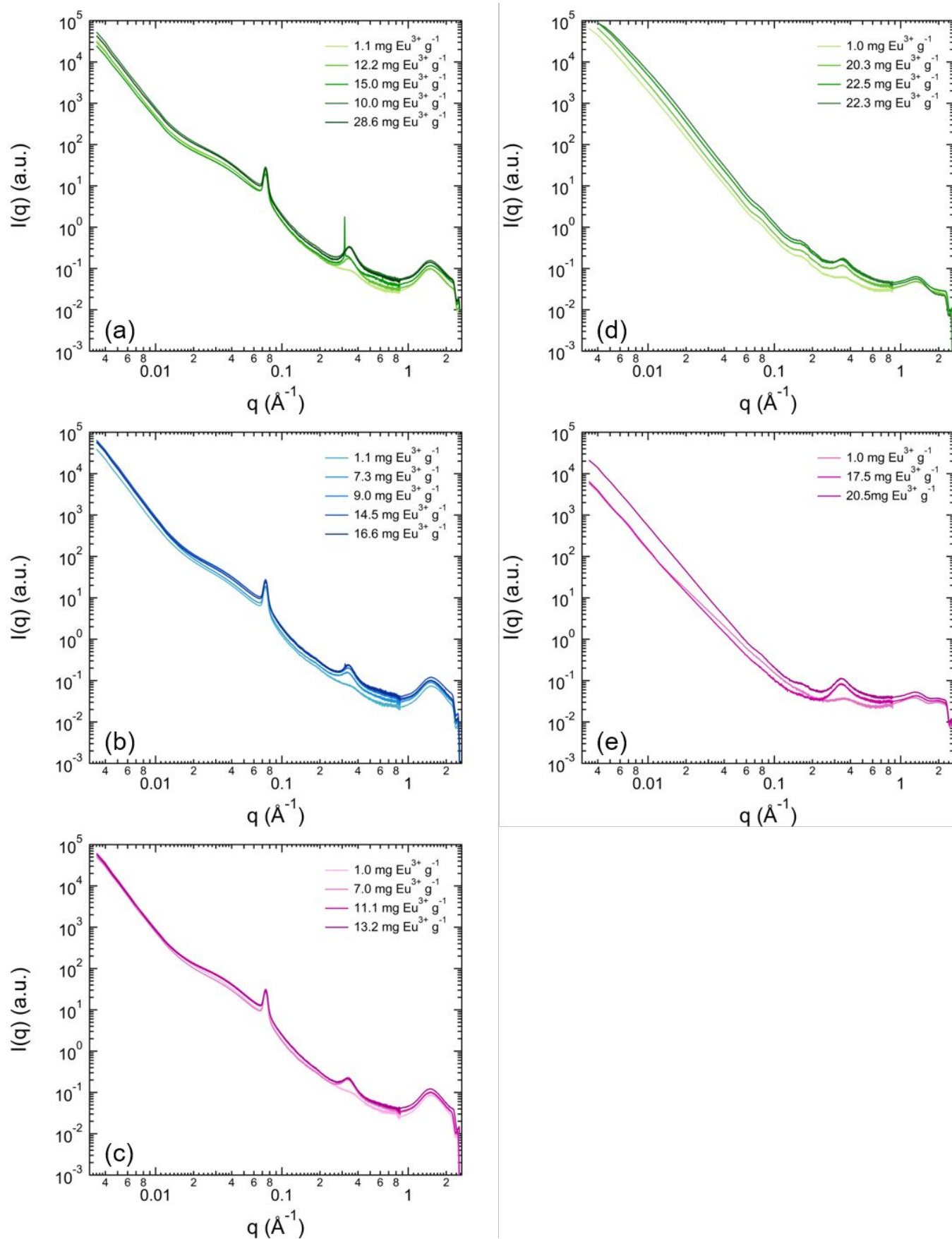


Figure 4. SAXS profiles for (a) 34 wt% TODGA OMC, (b) 22 wt% TODGA/4 wt% 2-octanol OMC, (c) 16 wt% TODGA/8 wt% 2-octanol OMC, (d) 40 wt% TODGA resin, and (e) 24 wt% TODGA/16 wt% 2-octanol resin with increasing Eu^{3+} loading.

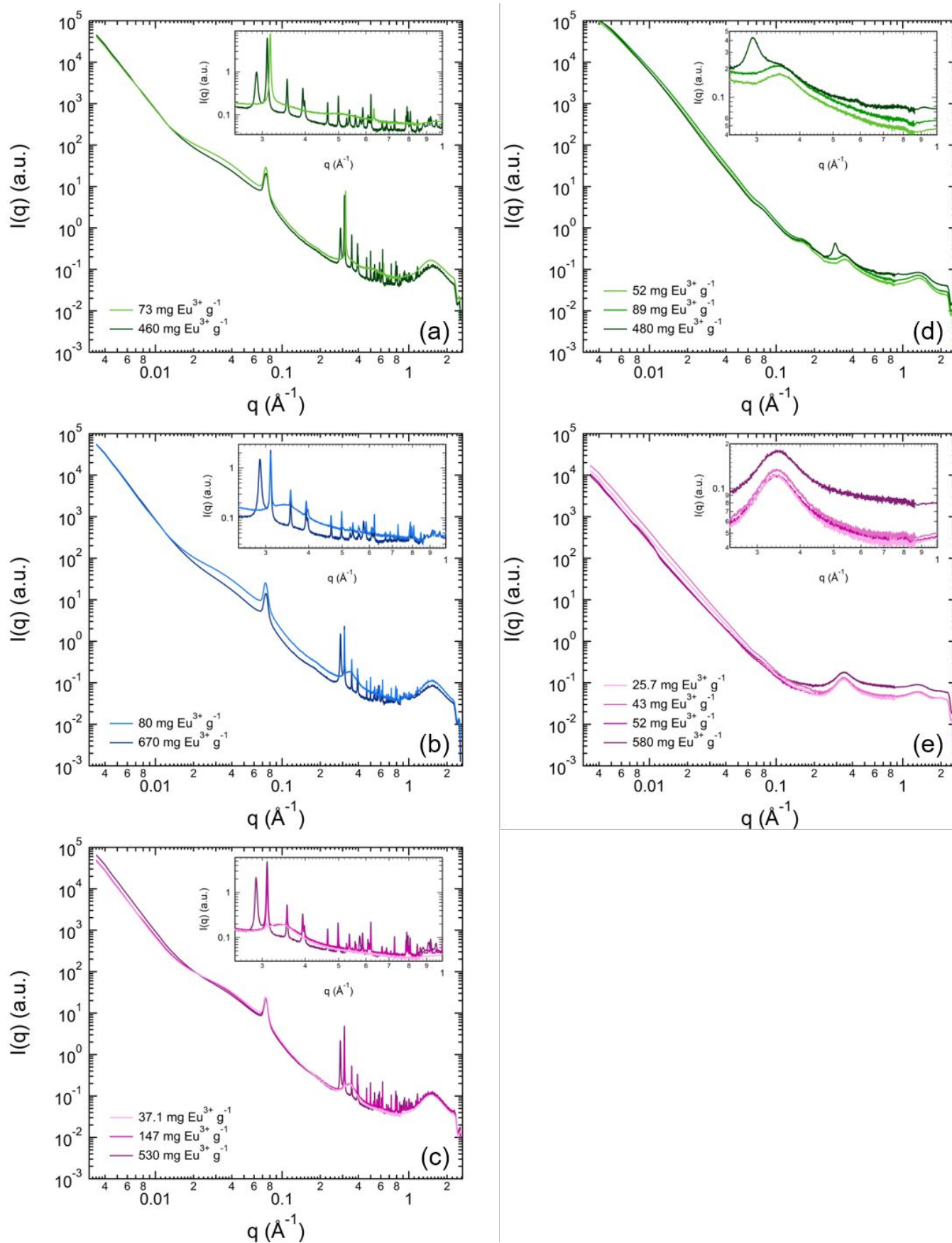


Figure 5. SAXS data for (a) 34 wt% TODGA OMC, (b) 22 wt% TODGA/4 wt% 2-octanol OMC, (c) 16 wt% TODGA/8 wt% 2-octanol OMC, (d) 40 wt% TODGA resin, and (e) 24 wt% TODGA/16 wt% 2-octanol resin with high Eu^{3+} loading. Insets show the diffraction region.

Eu³⁺ loadings, indicating the transition to the microcrystalline-like domain as shown in Figure 5a–c. Precedent for this type of non-crystalline to microcrystalline phase transition has been observed by SAXS studies of the pore confinement of polyoxoanion complexes in mesoporous materials.⁴³ The process is colloquially referred to as “ship-in-a-bottle” synthesis.^{44, 45}

Modelling of the microcrystalline systems was attempted using the crystallography data analysis software GSAS-II⁴⁶ and generalized indirect FT (GIFT).^{47–49} The fittings were vitiated because of the intricate comingling of the form factors and the structure factors due to polydispersity. Further, real space perspectives about the structures could not be obtained using GIFT due to the complexity of the data arising from polydispersity of particle scattering.

X-ray absorption spectroscopy

The oxygen phase-shift-corrected Fourier transform (FT) data of the $k^3\chi(k)$ EXAFS for the functionalized OMC and resin loaded with varying amounts of Eu³⁺ are shown in Figures 6 and 7. The prominent peak at approx. 2.4 Å is typical of inner-sphere oxygen bonding to Eu³⁺.^{17, 19, 24, 50–52} To account for this interaction, curve fitting was started with the most conservative model available. A single-shell fit (with three independent variables) for each of the $k^3\chi(k)$ EXAFS was done using a fixed O coordination number of 9. The results are given in Table 2 (see Figures S4–S8 for fit plots). As the Eu³⁺ concentration is increased, past the 1:3 Eu³⁺ to TODGA stoichiometric ratio, the Eu–O bond distance becomes elongated by up to 0.04 Å in the most concentrated samples. The Eu–O bond elongation does not appear to follow strict mole ratio or mass loading parameters. For example, three materials with approximate 1:1 Eu³⁺ to TODGA mole ratios and comparative Eu³⁺ mass loadings, 34 wt% TODGA OMC (73 mg Eu³⁺ g⁻¹), 22 wt% TODGA/4 wt% 2-octanol OMC (80 mg Eu³⁺ g⁻¹), and 40 wt% TODGA resin (89 mg Eu³⁺ g⁻¹), do not have equivalent Eu–O bond distances. Here, the 34 wt% TODGA OMC retains the shorter Eu–O bond distance while the other two materials begin to show Eu–O bond elongation. Further, the 34 wt% TODGA OMC and 22 wt% TODGA/4 wt% 2-octanol OMC materials have diffraction peaks in their SAXS profiles (see Figure 5a and b), whereas the 40 wt% TODGA resin does not (Figure 5d).

Beyond the principal peak at 2.4 Å, successive peaks at approx. 3.35 and 3.55 Å are present. These twin peaks are typically attributed to the sp²- and sp³-hybridized carbons related to the carbonyl (C_a) and ether (C_b) moieties, respectively, in TODGA (see Figure 1). Using structural precedence for the common homoleptic Eu(TODGA)₃³⁺ motif,^{19, 24} three-shell fits were done to describe Eu–O, Eu–C_a, and Eu–C_b interactions with fixed coordination numbers of 9 O, 6 C_a, and 6 C_b. The best fits adequately describe the Eu³⁺ coordination environments for all EXC materials with low Eu³⁺ loadings only. The refined fit parameters (Table 3, Figures S4–S8) are in good agreement with previous EXAFS characterizations of homoleptic Eu(TODGA)₃³⁺ complexes^{19, 24} from LLE. The three-shell model with fixed coordination numbers (O,C,C = 9,6,6) was inadequate to describe the EXAFS

for the higher Eu³⁺ concentrations. The O phase-shift-corrected FT data in Figures 6 and 7 show the diminution of the twin carbon peaks, particularly at the highest Eu³⁺ loading where the signal intensity is basically at background levels. The consistent presence of a distant feature at approx. 4.1 Å in the O phase-shift-corrected FT data in all the materials, with a peak intensity that becomes as great—if not greater—than the twin carbon features, indicates a physical significance of the feature with increasing Eu³⁺ concentration.

To probe the changing speciation and possible mesophase formation within the materials with the highest Eu³⁺ concentrations, alternate models were employed for the EXAFS fitting. The Eu–O coordination number was retained at 9; however, the two carbon coordination shells (C_a and C_b) were fit by floating integer coordination numbers and one Debye-Waller factor. The results were evaluated by the goodness of fit indices and, especially, the return of physically reasonable (e.g., non-negative) Debye-Waller factors. The coordination numbers found for Eu–C_a and Eu–C_b were then fixed. A fourth shell was added to identify and account for the most distant feature at approximately 4 Å in the FT data of Figures 6 and 7 (see curves (vi)) by performing a series of best Z fits by letting all variables float (N, r, and σ²). Two of the materials, 22 wt% TODGA/4 wt% 2-octanol OMC and 40 wt% TODGA resin, could not be fit using the four-shell model. The parameters obtained from the best fits of the other systems are given in Table 4 (see Figures S4–S8). In these fits, as the Eu³⁺ concentration increases, the presence of Eu–Eu interactions just above 4.0 Å for both OMC and resin materials have been identified. The transition to having Eu–Eu associations is directly correlated with the appearance of diffraction peaks in the OMC SAXS profiles, see Figure 5a–c (dark green, dark blue, and dark pink curves, respectively). With the Eu–Eu interactions, the Eu–C_a and Eu–C_b coordination numbers decrease as the contribution of the mononuclear Eu(TODGA)₃³⁺ response to the total Eu EXAFS signal decreases with the predominance of multinuclear Eu speciation. The decrease in Eu–C_a and Eu–C_b coordination numbers can be attributed to an increase in the Eu³⁺ to TODGA ratio. Recently, a LLE study using TODGA in an aromatic diluent found > 1:3 La³⁺ to TODGA stoichiometry through a metal loading isotherm and a 1:2 Eu³⁺–TODGA complex using time-resolved laser fluorescence spectroscopy.⁵³ The 1:2 Eu–TODGA species is made possible through heteroleptic complexation with nitrate and/or water. Because the Eu–O first shell is best fit by a coordination number of 9 in the EXAFS, a heteroleptic complex is also expected.

Collectively these findings—along with the shift in the electrode potential for the reduction of Eu³⁺ in the high Eu³⁺ loaded functionalized OMC materials reported in a previous study³⁶—suggest that TODGA and TODGA/2-octanol functionalized OMC materials undergo a non-crystalline to crystalline phase transition driven by the adsorption of hyperstoichiometric Eu³⁺ concentrations. The TODGA and TODGA/2-octanol functionalized resin materials are also capable of hyperstoichiometric Eu³⁺ absorption and demonstrate Eu–Eu interactions at high Eu³⁺ loading. But, unlike the OMC systems, the SAXS data (Figure 5d and e) provide no

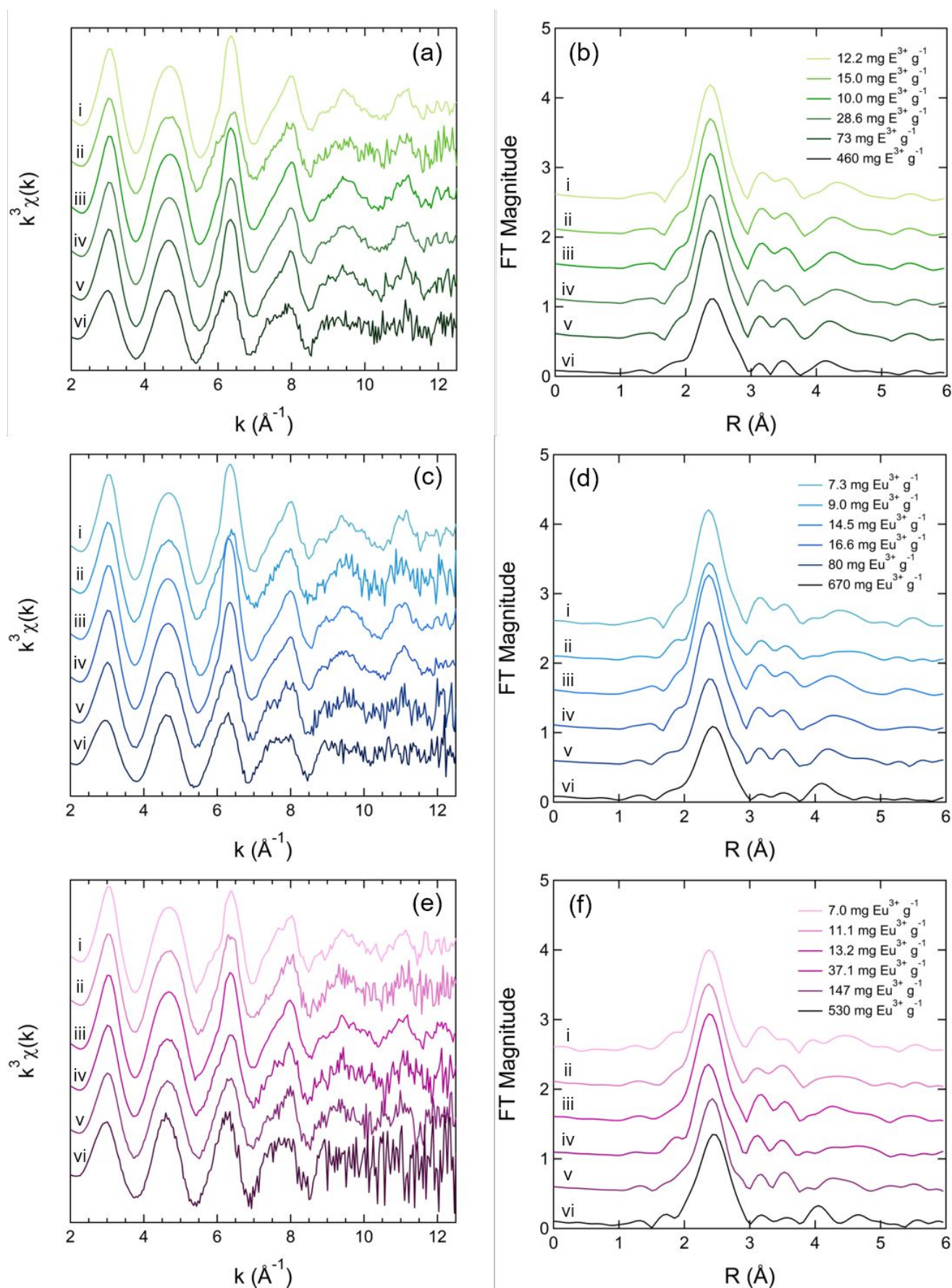


Figure 6. Eu L₃-edge $k^3\chi(k)$ EXAFS data (left) and the corresponding O phase-shift-corrected Fourier transform (FT) data (right) for (a,b) 34 wt% TODGA OMC, (c,d) 22 wt% TODGA/4 wt% 2-octanol OMC, and (e,f) 16 wt% TODGA/8 wt% 2-octanol OMC with increasing Eu³⁺ loadings from (i) to (vi). EXAFS data are arbitrarily offset for clarity.

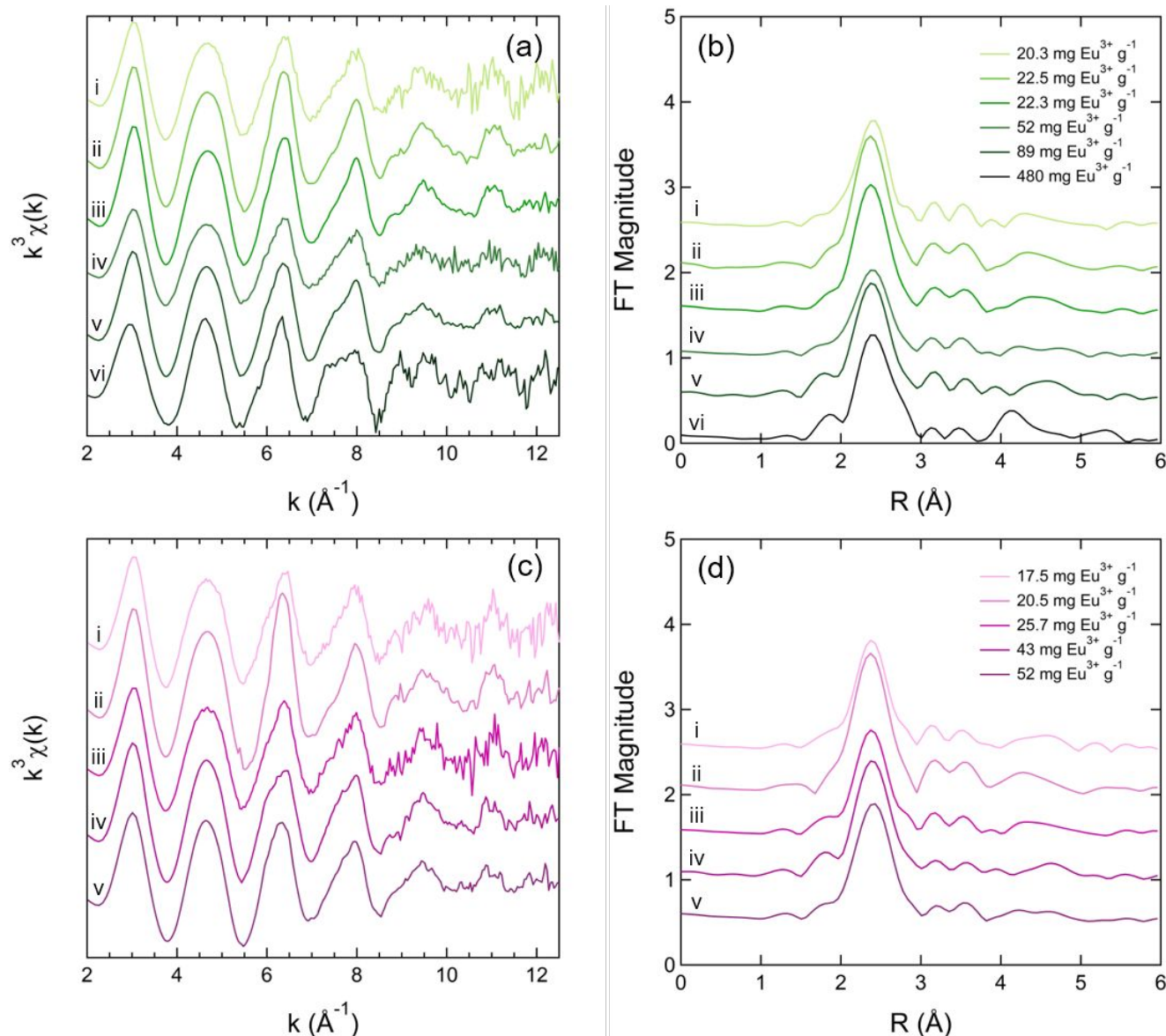


Figure 7. Eu L_{3} -edge $k^3\chi(k)$ EXAFS data (left) and corresponding O phase-shift-corrected FT data (right) for (a,b) 40 wt% TODGA resin and (c,d) 24 wt% TODGA/16 wt% 2-octanol resin with increasing Eu³⁺ loadings from (i) to (vi). EXAFS data are arbitrarily offset for clarity.

evidence for the formation of microcrystalline absorbates. The similarities in the Eu³⁺ adsorption properties and Eu coordination environments between the functionalized OMC and resin materials indicate that a mesophase consisting of multinuclear Eu topologies is present for the resin material. However, the larger pore sizes (and their broader distribution) for the resin inhibits the formation of microcrystalline-like domains. In contrast, Eu confinement within the smaller pore sizes (and their narrower distribution) for the OMC promotes and enhances crystalline nucleation. Precedent for exactly this type of phenomenon is provided by Shah et al.⁵⁴ who report selective protein crystallization in ordered mesoporous systems having narrow pore size distributions.

At low Eu³⁺ loadings, the Eu coordination environments for the OMC and resin materials resemble the LLE systems, supporting the formation of discrete, molecular Eu(TODGA)₃³⁺ complexes in EXC systems. When the Eu³⁺ loading is increased beyond the hyperstoichiometric 1:3 Eu³⁺ to TODGA ratio,

signature diffraction peaks appear and the local Eu coordination environment changes—having less carbon interactions and having multinuclear Eu speciation. This structure of this mesophase—although not fully identified—diverges from the discrete molecular cation complex, Eu(TODGA)₃³⁺, notably by the presence of Eu–Eu correlations that are diagnostic of a multinuclear entity, whose contribution to the EXAFS does not completely obscure the molecular TODGA complex.

Because EXAFS captures an average of all the surroundings of all the Eu present in the system, it is difficult to make an absolute assertion on the extent of Eu–TODGA complexation and Eu-mesophase domain structures attributable to the formation of reverse-admicelles under high Eu³⁺ loading conditions. In some liquid-solid separations (chromatography), admicelles are used to increase the solubilization of nonpolar solutes within an oleophilic core.^{55, 56} In this scenario with TODGA, a hydrophilic, fluid-like environment would be created in the reverse-admicelle core, composed of an undefined

number of TODGA molecules. The fluid-like environment would consist of extracted Eu^{3+} , NO_3^- , HNO_3 , and water. At the highest Eu^{3+} loadings in the OMC materials, this fluid-like environment may begin to condense causing the microcrystalline-like SAXS diffraction peaks. In LLE, the analogous process of phase

separation is known as third phase formation, a deleterious phenomenon that TODGA is susceptible to when contacted with high concentrations of Eu^{3+} and other trivalent lanthanide ions.^{28, 32, 53, 57-59}

Table 2. Europium EXAFS one-shell fit summary. The Eu–O coordination number was fixed at 9. The average Eu–O distance is given before bond elongation for a straightforward comparison. The shorter Eu–O distances are the same for all materials within error.

	Eu^{3+} (mg g ⁻¹)	ΔE_0 (eV)	r (Å)	Eu–O	
				r_{avg} (Å)	σ^2 (Å ²)
34 wt% TODGA OMC	12.2	–2.5(4)	2.394(4)	2.399(8)	0.0084(3)
	15.0	–2.2(5)	2.405(5)		0.0106(4)
	10.0	–2.3(4)	2.397(3)		0.0083(3)
	28.6	–2.4(4)	2.398(3)		0.0090(3)
	73	–2.3(4)	2.403(4)		0.0090(3)
	460	–1.6(5)	2.431(5)		0.0117(4)
22 wt% TODGA/4 wt% 2-octanol OMC	7.3	–2.6(4)	2.392(4)	2.397(8)	0.0084(3)
	9.0	–2.5(5)	2.400(4)		0.0092(3)
	14.5	–2.6(5)	2.394(4)		0.0078(3)
	16.6	–2.4(4)	2.400(3)		0.0091(3)
	80	–2.2(2)	2.411(5)		0.0104(4)
	670	–1.3(4)	2.441(5)		0.0117(4)
16 wt% TODGA/8 wt% 2-octanol OMC	7.0	–2.2(4)	2.399(4)	2.399(8)	0.0100(3)
	11.1	–2.6(5)	2.395(4)		0.0086(3)
	13.2	–2.2(4)	2.399(4)		0.0092(3)
	37.1	–2.6(5)	2.403(5)		0.0099(4)
	147	–1.5(5)	2.420(5)		0.0097(4)
	530	–0.5(8)	2.448(8)		0.0092(7)
40 wt% TODGA resin	20.3	–2.2(4)	2.402(4)	2.398(8)	0.0107(4)
	22.5	–2.8(4)	2.392(3)		0.0090(3)
	22.3	–2.5(3)	2.395(3)		0.0096(2)
	52	–2.3(4)	2.405(4)		0.0133(4)
	89	–1.9(3)	2.411(3)		0.0107(2)
	480	–1.5(5)	2.431(5)		0.0102(4)
24 wt% TODGA/16 wt% 2-octanol resin	17.5	–2.5(5)	2.398(4)	2.396(7)	0.0104(4)
	20.5	–2.8(4)	2.391(4)		0.0085(3)
	25.7	–2.5(4)	2.400(4)		0.0108(4)
	43	–1.8(3)	2.411(3)		0.0106(2)
	52	–1.6(2)	2.414(2)		0.0104(2)

Table 3. Europium EXAFS three-shell fit summary for selected materials. Coordination numbers were fixed at 9 O, 6 C_a, and 6 C_b. A single Debye-Waller factor (σ^2) was refined for both C_a and C_b. A single energy threshold parameter (ΔE_0) was used for all three shells.

	Eu ³⁺ (mg g ⁻¹)	ΔE_0 (eV)	Eu–O		Eu–C _a		Eu–C _b
			r (Å)	σ^2 (Å ²)	r (Å)	σ^2 (Å ²)	r (Å)
34 wt% TODGA OMC	12.2	–1.6(3)	2.398(2)	0.0084(2)	3.361(8)	0.0048(8)	3.541(8)
	15.0	–1.8(3)	2.403(4)	0.0107(3)	3.296(8)	0.0054(7)	3.524(9)
	10.0	–1.5(3)	2.400(2)	0.0084(2)	3.358(8)	0.0058(9)	3.547(9)
	28.6	–1.8(3)	2.402(3)	0.0090(2)	3.359(8)	0.0065(9)	3.558(9)
	73	–2.1(3)	2.406(3)	0.0090(2)	3.37(1)	0.008(2)	3.56(1)
22 wt% TODGA/ 4 wt% 2-octanol OMC	7.3	–1.8(3)	2.396(3)	0.0084(2)	3.351(8)	0.0047(8)	3.538(8)
	9.0	–1.8(3)	2.403(3)	0.0092(3)	3.35(1)	0.008(1)	3.56(1)
	14.5	–1.7(3)	2.398(3)	0.0078(3)	3.367(8)	0.0033(8)	3.545(9)
	16.6	–1.6(3)	2.404(3)	0.0092(2)	3.37(1)	0.008(2)	3.55(1)
16 wt% TODGA/ 8 wt% 2-octanol OMC	7.0	–1.5(3)	2.402(3)	0.0100(3)	3.35(1)	0.007(1)	3.55(1)
	11.1	–1.8(4)	2.400(3)	0.0087(3)	3.37(2)	0.009(3)	3.55(2)
	13.2	–1.7(2)	2.401(2)	0.0092(2)	3.337(6)	0.0049(6)	3.537(7)
	37.1	–2.3(4)	2.403(4)	0.0100(4)	3.31(1)	0.008(1)	3.53(2)
	147	–1.3(4)	2.419(4)	0.0097(4)	3.32(1)	0.006(1)	3.55(1)
40 wt% TODGA resin	20.3	–1.8(3)	2.402(3)	0.0107(3)	3.322(9)	0.0064(9)	3.54(1)
	22.5	–1.8(2)	2.396(2)	0.0091(2)	3.358(8)	0.008(1)	3.556(9)
	22.3	–1.7(2)	2.399(2)	0.0096(2)	3.359(8)	0.008(1)	3.566(9)
	52	–1.3(3)	2.411(4)	0.0134(3)	3.43(4)	0.02(1)	3.60(7)
	89	–1.2(2)	2.416(3)	0.0107(2)	3.41(2)	0.020(6)	3.61(3)
24 wt% TODGA/ 16 wt% 2-octanol resin	17.5	–2.1(3)	2.399(4)	0.0104(3)	3.32(1)	0.009(1)	3.55(1)
	20.5	–1.9(3)	2.396(3)	0.0085(2)	3.366(8)	0.0046(8)	3.553(8)
	25.7	–1.8(3)	2.403(4)	0.0109(3)	3.35(1)	0.009(2)	3.57(1)
	43	–1.1(2)	2.415(3)	0.0106(2)	3.40(2)	0.020(4)	3.65(2)

Conclusions

At high Eu³⁺ loadings, in which the Eu³⁺ to TODGA ratio is greater than 1:3, the hyperstoichiometric Eu³⁺—in excess of the TODGA saturation where all the TODGA is bound to Eu³⁺ in the form of the Eu(TODGA)₃³⁺ coordination complex—adsorbs to the solid supports as reverse-admicelles. From a microscopic perspective of Eu³⁺, the presence of mixed speciation diminishes the signatures for the coordination complex, leading to elongated Eu–O inner (first) coordination sphere distances and diminished intensities of the outer sphere Eu–C_a and Eu–C_b peaks due to the carbonyl sp²-hybridized carbon (second coordination sphere) and the sp³-hybridized carbon adjacent to the ether O (third coordination sphere). Additional, distant backscattering is observed that is consistent with a fourth coordination sphere of Eu, suggesting the presence of a multinuclear entity. At the mesoscopic level, the influence of material properties is evident especially in terms of the pore size and pore ordering, both of which play a role in creating microcrystalline-like domains of Eu³⁺ with OMC. No such domains are templated by the disordered pore distributions of the resin. The ability to tune the

support material porosity for solid-liquid separations—facilitating the crystallization of a selected cation from a mixed solution—opens new opportunities for research and engineering in EXC.

Conflicts of interest

The authors declare no conflicts of interest.

Table 4. Europium EXAFS fit summary for high Eu³⁺ loaded materials. The coordination number for O was fixed at 9. The coordination numbers for C_a and C_b were fixed after initial refinement (see text for details). A single Debye-Waller factor (σ^2) was refined for both C_a and C_b. The final shell was fit with multiple likely elements. The best refined fit is shown.

	Eu ³⁺ (mg g ⁻¹)	ΔE_0 (eV)	Eu–O			Eu–C _a			Eu–C _b		Eu–X			
			N	r (Å)	σ^2 (Å ²)	N	r (Å)	σ^2 (Å ²)	N	r (Å)	X	N	r (Å)	σ^2 (Å ²)
34 wt% TODGA OMC	28.6	-1.5(2)	9	2.403(2)	0.0090(2)	4	3.354(7)	0.0046(6)	5	3.544(6)	C	6.6(9)	4.382(5)	0.004(1)
	73	-1.6(2)	9	2.407(2)	0.0090(2)	3	3.35(1)	0.0034(7)	5	3.540(7)	Eu	5.1(9)	4.050(6)	0.013(1)
	460	-1.7(7)	9	2.427(6)	0.0084(6)	2	3.39(4)	0.002(2)	4	3.57(2)	Eu	6(2)	4.04(1)	0.011(2)
22 wt% TODGA/ 4 wt% 2-octanol OMC	16.6	-1.6(2)	9	2.404(2)	0.0092(2)	3	3.34(1)	0.0042(7)	5	3.52(1)	C	8(1)	4.382(6)	0.005(1)
	80	-1.7(4)	9	2.414(4)	0.0105(3)	2	3.34(2)	0.0022(9)	4	3.54(1)	Eu	3.7(9)	4.029(8)	0.010(2)
	672*	-1.1(4)	9	2.442(4)	0.0117(3)	2	3.59(1)	0.003(2)	—	—	Eu	3.1(8)	4.031(8)	0.010(2)
16 wt% TODGA/ 8 wt% 2-octanol OMC	37	-2.1(4)	9	2.405(4)	0.0100(3)	3	3.30(1)	0.003(1)	4	3.51(1)	C	8(2)	4.37(1)	0.007(3)
	147	-1.1(3)	9	2.421(4)	0.0098(3)	3	3.33(1)	0.0028(7)	5	3.548(8)	Eu	4(1)	4.05(1)	0.012(2)
	533	-0.7(8)	9	2.446(8)	0.0092(6)	1	3.40(7)	0.002(5)	2	3.59(4)	Eu	6(3)	4.05(2)	0.016(6)
40 wt% TODGA resin	89	-1.4(2)	9	2.413(2)	0.011(2)	3	3.348(8)	0.0061(8)	4	3.560(7)	C	5.9(8)	4.371(5)	0.005(1)
	326	-1.7(4)	9	2.429(4)	0.010(3)	—	—	—	—	—	Eu	4.6(8)	4.042(6)	0.010(1)
24 wt% TODGA/ 16 wt% 2-octanol resin	43	-1.2(2)	9	2.414(2)	0.0106(2)	3	3.36(1)	0.008(1)	4	3.60(1)	C	3.2(8)	4.391(9)	0.003(2)
	52	-1.1(1)	9	2.418(1)	0.0104(1)	2	3.386(8)	0.0043(5)	4	3.587(5)	Eu	2.5(4)	4.071(5)	0.012(1)

*The 22 wt% TODGA/4 wt% 2-octanol OMC loaded with 672 mg Eu³⁺ g⁻¹ fit best using a four-shell model without carbon interactions. This model retained the fixed coordination number of 9 for O in the first shell. The coordination numbers for the second shell (Eu–N) was fixed to 2 after initial refinement. The third coordination shell was set to describe Eu–Eu interactions, with a refined coordination number of 2(1). The coordination number for the fourth coordination shell (Eu–O_{distal}) was set equal to Eu–N, relating to the distal oxygen of bidentate nitrate coordination. The refined distances for Eu–O, Eu–N, Eu–Eu, and Eu–O_{distal} are 2.440(4), 2.92(1), 4.01(2), and 4.38(5) Å, respectively, with Debye-Waller factors (σ^2) of 0.0118(3), 0.006(2), 0.008(3), and 0.007(8) Å². The refined energy shift (ΔE_0) is -1.8(5) eV.

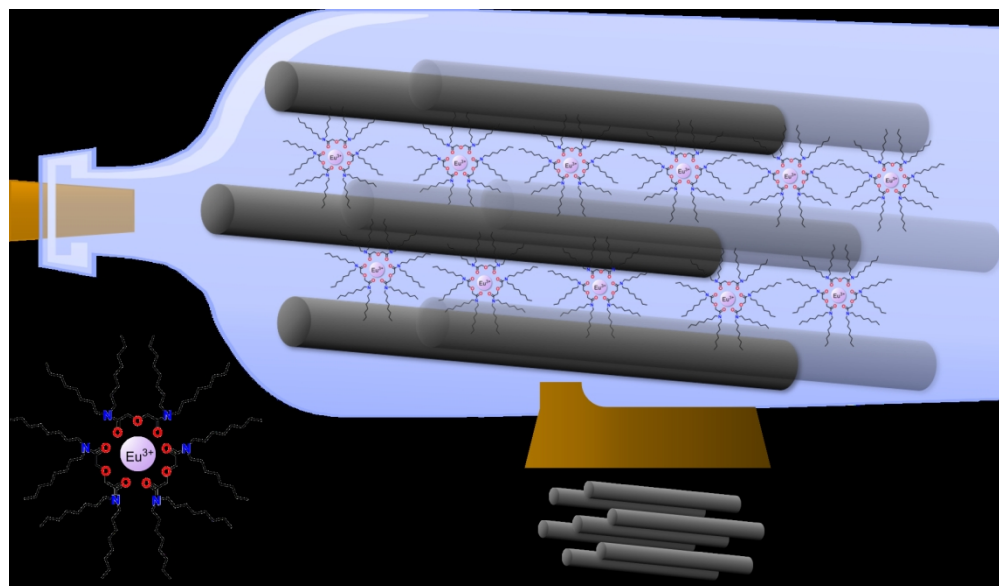
Acknowledgements

This research was performed on beamlines at Sector 12 of the APS, a DOE Office of Science User Facility operated for the DOE Office of Science by Argonne National Laboratory, which is supported under Contract No. DE-AC02-06CH11357. We thank Dr. Xiaobing Zuo at 12-ID-B. We also thank Dr. Daniel McAlister at Eichrom Technologies, LLC. for providing the resin materials. Dr. Mark Antonio acknowledges support from the Office of Basic Energy Sciences, Division of Chemical Sciences, Biosciences and Geosciences under Contract No. DE-AC02-06CH11357. The Colorado School of Mines authors acknowledge the funding provided by the Defense Threat Reduction Agency (DTRA) under grant number HDTRA1-16-0015. This work was also based upon support provided to E. R. Bertelsen by the U.S. Department of Energy, Office of Science Graduate Student Research (SCGSR) Program.

References

- 1 S. Cotton, in *Lanthanide and Actinide Chemistry*, eds. D. Woollins, B. Crabtree, D. Atwood and M. Gerd, John Wiley & Sons Ltd., West Sussex, England, 2006, ch. 1, p. 4.
- 2 C. James, *J. Am. Chem. Soc.*, 1911, **33**, 1332-1344.
- 3 Y. Sasaki, Y. Sugo, S. Suzuki and S. Tachimori, *Solvent Extr. Ion Exch.*, 2001, **19**, 91-103.
- 4 Z.-X. Zhu, Y. Sasaki, H. Suzuki, S. Suzuki and T. Kimura, *Anal. Chim. Acta*, 2004, **527**, 163-168.
- 5 E. A. Mowafy and H. F. Aly, *Solvent Extr. Ion Exch.*, 2007, **25**, 205-224.
- 6 S. A. Ansari, P. Pathak, P. K. Mohapatra and V. K. Manchanda, *Chem. Rev.*, 2012, **112**, 1751-1772.
- 7 A. V. Gelis and G. J. Lumetta, *Ind. Eng. Chem. Res.*, 2014, **53**, 1624-1631.
- 8 G. J. Lumetta, A. V. Gelis, J. C. Carter, C. M. Niver and M. R. Smoot, *Solvent Extr. Ion Exch.*, 2014, **32**, 333-347.
- 9 B. J. Gullekson, M. A. Brown, A. Paulenova and A. V. Gelis, *Ind. Eng. Chem. Res.*, 2017, **56**, 12174-12183.
- 10 D. Whittaker, A. Geist, G. Modolo, R. Taylor, M. Sarsfield and A. Wilden, *Solvent Extr. Ion Exch.*, 2018, **36**, 223-256.
- 11 M. Carrott, A. Geist, X. Hères, S. Lange, R. Malmbeck, M. Miguiritchian, G. Modolo, A. Wilden and R. Taylor, *Hydrometallurgy*, 2015, **152**, 139-148.
- 12 M. Carrott, K. Bell, J. Brown, A. Geist, C. Gregson, X. Hères, C. Maher, R. Malmbeck, C. Mason, G. Modolo, U. Müllich, M. Sarsfield, A. Wilden and R. Taylor, *Solvent Extr. Ion Exch.*, 2014, **32**, 447-467.
- 13 R. Taylor, M. Carrott, H. Galan, A. Geist, X. Hères, C. Maher, C. Mason, R. Malmbeck, M. Miguiritchian, G. Modolo, C. Rhodes, M. Sarsfield and A. Wilden, *Procedia Chem.*, 2016, **21**, 524-529.
- 14 D. Magnusson, A. Geist, R. Malmbeck, G. Modolo and A. Wilden, *Procedia Chem.*, 2012, **7**, 245-250.
- 15 A. Wilden, G. Modolo, M. Sypula, A. Geist and D. Magnusson, *Procedia Chem.*, 2012, **7**, 418-424.
- 16 G. Modolo, A. Wilden, P. Kaufholz, D. Bosbach and A. Geist, *Prog. Nucl. Energy*, 2014, **72**, 107-114.
- 17 D. M. Brigham, A. S. Ivanov, B. A. Moyer, L. H. Delmau, V. S. Bryantsev and R. J. Ellis, *J. Am. Chem. Soc.*, 2017, **139**, 17350-17358.
- 18 S. D. Reilly, A. J. Gaunt, B. L. Scott, G. Modolo, M. Iqbal, W. Verboom and M. J. Sarsfield, *Chem. Commun.*, 2012, **48**, 9732-9734.
- 19 M. R. Antonio, D. R. McAlister and E. P. Horwitz, *Dalton Trans.*, 2015, **44**, 515-521.
- 20 R. J. Ellis, M. K. Bera, B. Reinhart and M. R. Antonio, *Phys. Chem. Chem. Phys.*, 2016, **18**, 31254-31259.
- 21 A. G. Baldwin, A. S. Ivanov, N. J. Williams, R. J. Ellis, B. A. Moyer, V. S. Bryantsev and J. C. Shafer, *ACS Cent. Sci.*, 2018, **4**, 739-747.
- 22 A. Sengupta, S. M. Ali and K. T. Shenoy, *Polyhedron*, 2016, **117**, 612-622.
- 23 A. Sengupta, A. Bhattacharyya, W. Verboom, S. M. Ali and P. K. Mohapatra, *J. Phys. Chem. B*, 2017, **121**, 2640-2649.
- 24 R. J. Ellis, D. M. Brigham, L. Delmau, A. S. Ivanov, N. J. Williams, M. N. Vo, B. Reinhart, B. A. Moyer and V. S. Bryantsev, *Inorg. Chem.*, 2017, **56**, 1152-1160.
- 25 M. P. Jensen, T. Yaita and R. Chiarizia, *Langmuir*, 2007, **23**, 4765-4774.
- 26 S. Nave, G. Modolo, C. Madic and F. Testard, *Solvent Extr. Ion Exch.*, 2004, **22**, 527-551.
- 27 P. N. Pathak, S. A. Ansari, P. K. Mohapatra, V. K. Manchanda, A. K. Patra and V. K. Aswal, *J. Colloid Interface Sci.*, 2013, **393**, 347-351.
- 28 K. Rama Swami, K. A. Venkatesan and M. P. Antony, *Ind. Eng. Chem. Res.*, 2018, **57**, 13490-13497.
- 29 R. B. Gujar, S. A. Ansari, D. R. Prabhu, P. N. Pathak, A. Sengupta, S. K. Thulasidas, P. K. Mohapatra and V. K. Manchanda, *Solvent Extr. Ion Exch.*, 2012, **30**, 156-170.
- 30 Y. Sasaki, Y. Sugo, K. Morita and K. L. Nash, *Solvent Extr. Ion Exch.*, 2015, **33**, 625-641.
- 31 P. N. Pathak, S. A. Ansari, S. Kumar, B. S. Tomar and V. K. Manchanda, *J. Colloid Interface Sci.*, 2010, **342**, 114-118.
- 32 Y. Sasaki, P. Rapold, M. Arisaka, M. Hirata, T. Kimura, C. Hill and G. Cote, *Solvent Extr. Ion Exch.*, 2007, **25**, 187-204.
- 33 M. A. Momen and M. L. Dietz, *Talanta*, 2019, **197**, 612-621.
- 34 J. L. Cortina, N. Miralles, M. Aguilar and A. M. Sastre, *Solvent Extr. Ion Exch.*, 1994, **12**, 371-391.
- 35 E. R. Bertelsen, G. Deodhar, K. T. Kluherz, M. Davidson, M. L. Adams, B. G. Trewyn and J. C. Shafer, *J. Chromatogr. A*, 2019, **1595**, 248-256.
- 36 E. R. Bertelsen, N. C. Kovach, B. G. Trewyn, M. R. Antonio and J. C. Shafer, *J. Mater. Chem. C*, 2020, **8**, 6689-6700.
- 37 E. P. Horwitz, D. R. McAlister, A. H. Bond and R. E. Barrans, *Solvent Extr. Ion Exch.*, 2005, **23**, 319-344.
- 38 J. A. Drader, L. Zhu, P. Smith, K. McCann, S. Boyes and J. C. Braley, *Sep. Purif. Technol.*, 2016, **163**, 352-356.
- 39 J. J. Rehr and R. C. Albers, *Rev. Mod. Phys.*, 2000, **72**, 621-654.
- 40 The effects of complex formation on electrode potentials are very well known.[see, for example, Laitinen, H. A.; Harris, W. E. In *Chemical Analysis: An Advanced Text and Reference*; 2nd ed.; McGraw-Hill: New York, 1975, p 230; Ringbom, A.; Wänninen, E. In *Treatise on Analytical Chemistry. Part 1: Theory and Practice*; 2nd ed.; Kolthoff, I. M.; Elving, P. J., Eds.; John Wiley & Sons: New York, 1979; Vol. 2, p 521.] Comparison of the electrode potentials for the aquated Eu(III) and the TODGA-complexed Eu(III) reflect the relative stabilities of the two systems. Here, the negative shift for the Eu-TODGA complex indicates that it is a more stable complex than the aquated cation.
- 41 M. Joglekar, S. Pylypenko, M. M. Otting, J. S. Valenstein and B. G. Trewyn, *Chem. Mater.*, 2014, **26**, 2873-2882.
- 42 *Journal*, 2007.
- 43 J. Juan-Alcañiz, M. Goesten, A. Martinez-Joaristi, E. Stavitski, A. V. Petukhov, J. Gascon and F. Kapteijn, *Chem. Commun.*, 2011, **47**, 8578-8580.
- 44 S. R. Mukai, M. Shimoda, L. Lin, H. Tamon and T. Masuda, *Appl. Catal., A*, 2003, **256**, 107-113.
- 45 E. V. Vinogradova, P. Müller and S. L. Buchwald, *Angew. Chem. Int. Ed.*, 2014, **53**, 3125-3128.

- 46 B. H. Toby and R. B. Von Dreele, *J. Appl. Crystallogr.*, 2013, **46**, 544-549.
- 47 G. Fritz, A. Bergmann and O. Glatter, *The Journal of Chemical Physics*, 2000, **113**, 9733-9740.
- 48 J. Brunner-Popela and O. Glatter, *J. Appl. Crystallogr.*, 1997, **30**, 431-442.
- 49 B. Weyerich, J. Brunner-Popela and O. Glatter, *J. Appl. Crystallogr.*, 1999, **32**, 197-209.
- 50 M. R. Antonio, J. Jing, B. P. Burton-Pye and L. C. Francesconi, *Dalton Trans.*, 2010, **39**, 7980-7992.
- 51 J. Jing, B. P. Burton-Pye, L. C. Francesconi and M. R. Antonio, *Inorg. Chem.*, 2008, **47**, 6889-6899.
- 52 I. Persson, E. Damian Risberg, P. D'Angelo, S. De Panfilis, M. Sandström and A. Abbasi, *Inorg. Chem.*, 2007, **46**, 7742-7748.
- 53 P. Weßling, U. Müllich, E. Guerinoni, A. Geist and P. J. Panak, *Hydrometallurgy*, 2020, **192**, 105248.
- 54 U. V. Shah, D. R. Williams and J. Y. Y. Heng, *Cryst. Growth Des.*, 2012, **12**, 1362-1369.
- 55 A. Charoensaeng, D. A. Sabatini and S. Khaodhiar, *J. Surfactants Deterg.*, 2009, **12**, 209-217.
- 56 J. W. Barton, T. P. Fitzgerald, C. Lee, E. A. O'Rear and J. H. Harwell, *Sep. Sci. Technol.*, 1988, **23**, 637-660.
- 57 S. Tachimori, Y. Sasaki and S.-i. Suzuki, *Solvent Extr. Ion Exch.*, 2002, **20**, 687-699.
- 58 G. Modolo, H. Asp, C. Schreinemachers and H. Vijgen, *Solvent Extr. Ion Exch.*, 2007, **25**, 703-721.
- 59 Y. Sasaki, Y. Sugo, S. Suzuki and T. Kimura, *Anal. Chim. Acta*, 2005, **543**, 31-37.



311x181mm (150 x 150 DPI)